A&A 650, A24 (2021)
https://doi.org/10.1051/0004-6361/202039352

Astronomy & Astrophysics

Parker Solar Probe: Ushering a new frontier in space exploration

Special issue

A new view of energetic particles from stream interaction regions observed by Parker Solar Probe

N. A. Schwadron[1,2], C. J. Joyce[2], A. Aly[1], C. M. S. Cohen[3], M. I. Desai[4], D. J. McComas[2], J. T. Niehof[1], E. Möbius[1], M. Lee[1], J. Bower[1], S. Bale[5], A. Case[6], E. R. Christian[7], A. J. Davis[3], W. de Wet[1], K. Goetz[5], J. Giacalone[8], M. E. Hill[9], R. Allen[9], J. C. Kasper[10,11], K. Korreck[6], R. A. Leske[3], O. Malandraki[12], W. H. Matthaeus[13], R. L. McNutt Jr.[9], R. A. Mewaldt[3], D. G. Mitchell[9], M. Pulupa[5], J. S. Rankin[2], E. C. Roelof[9], E. C. Stone[3], J. R. Szalay[2], and M. E. Wiedenbeck[14]

[1] University of New Hampshire, Durham, NH 03824, USA
e-mail: nschwadron@unh.edu
[2] Department of Astrophysical Sciences, Princeton University, Princeton, NJ 08544, USA
[3] California Institute of Technology, Pasadena, CA 91125, USA
[4] University of Texas at San Antonio, San Antonio, TX 78249, USA
[5] University of California at Berkeley, Berkeley, CA 94720, USA
[6] Harvard-Smithsonian Center for Astrophysics, Cambridge, MA 02138, USA
[7] Goddard Space Flight Center, Greenbelt, MD 20771, USA
[8] University of Arizona, Tucson, AZ 85721, USA
[9] Johns Hopkins University, Applied Physics Laboratory, Laurel, MD 20723, USA
[10] BWX Technologies, Inc, Lynchburg, VA, 24504, USA
[11] University of Michigan, Ann Arbor, MI 48109, USA
[12] Institute for Astronomy, Astrophysics, Space Applications and Remote Sensing of the National Observatory of Athens, Vas. Pavlou and I. Metaxa, 15236 Penteli, Greece
[13] University of Delaware, Newark, DE 19716, USA
[14] Jet Propulsion Laboratory, California Institute of Technology, Pasadena, CA 91109, USA

Received 7 September 2020 / Accepted 14 November 2020

ABSTRACT

Early observations from the first orbit of Parker Solar Probe (PSP) show recurrent stream interaction regions that form close to the Sun. Energetic particle enhancements were observed on the 320th–326th day of the year 2018, which corresponds to ~1–7 days after the passage of the stream interface between faster and slower solar wind. Energetic particles stream into the inner heliosphere to the PSP spacecraft near 0.33 au (71 solar radii) where they are measured by the Integrated Science Investigation of the Sun (IS⊙IS). The large 6-day time interval over which energetic particles are observed after the stream passage provides a unique perspective on the development of stream interactions within the heliosphere. The long duration of energetic particle enhancements suggests that particles stream in through the inner heliosphere more directly along magnetic field lines that form a sub-Parker spiral structure due to magnetic footpoint motion at the Sun and shearing of the magnetic field in the rarefaction region behind the stream interface. The strong build-up of energetic particle fluxes in the first 3 days after the passage of the stream interface indicates that suprathermal populations are enhanced near the interaction region through compression or other acceleration processes in addition to being diffusively accelerated. The early increases in energetic particle fluxes (in the first 3 days) in the formation of these events allows for the characterization of the acceleration associated with these suprathermal seed populations. Thus, we show that the time history of energetic particle fluxes observed by IS⊙IS provides a new view of particle acceleration at stream interaction regions throughout the inner heliosphere.

Key words. Sun: magnetic fields – solar wind – Sun: heliosphere – shock waves – acceleration of particles

1. Introduction

The NASA Parker Solar Probe (PSP) mission explores our nearest star, the Sun, and its environment (Fox et al. 2016). Comprehensive measurements of solar energetic particles (SEPs) are provided by the Integrated Science Investigation of the Sun (IS⊙IS) instrument suite (McComas et al. 2016), which is comprised of two Energetic Particle Instruments measuring Higher (EPI-Hi) and Lower (EPI-Lo) energy particles (McComas et al. 2016) over the range 0.02–200 MeV/nucleon. Here, we examine energetic particles accelerated from stream interaction regions in the inner heliosphere, at radial distances beyond the PSP spacecraft (to ~5 au). The stream interfaces were identified using in situ plasma observations from the Solar Wind Electrons Alphas and Protons Investigation (SWEAP; Kasper et al. 2016) and the in situ magnetic field observations from the electromagnetic fields investigation, commonly referred to as FIELDS (Bale et al. 2016).

Particles with energies on the order of 1 MeV per nucleon are accelerated at the forward and reverse shocks and compressive waves that bound corotating interaction regions (CIRs; e.g. Barnes & Simpson 1976; McDonald et al. 1976; Fisk & Lee 1980) and stream interaction regions (SIRs). These interaction regions are formed from faster corotating solar wind streams

overtaking slower solar wind streams. Typically, it is assumed that CIRs and SIRs accelerate particles beyond several au, where shocks are generally formed. However, observational studies at 1 au by Wind have shown that CIR ions are first accelerated much closer to the Sun (within 1.5 au) than previously thought (Chotoo et al. 2000; Mason 2000; Giacalone et al. 2002), and the suprathermal populations that feed into the acceleration process are largely composed of interstellar pickup ions (e.g., Schwadron et al. 1996). The conclusion that CIR acceleration begins near 1 au is supported by observations from SOHO and ACE (Yu et al. 2017).

One of the puzzles that has surrounded the acceleration of CIR particles closer to the Sun, at less than 1.5 au, is whether the acceleration process requires the presence of well-defined and relatively strong shocks (Chotoo et al. 2000). The modeling of pickup ions and a comparison with observations from STEREO shows that the acceleration process and the development of relatively hard suprathermal tails begins where CIR compression regions are first formed inside of 1 au (Chen et al. 2015).

An important feature of energetic particles in SIRs is that the energy spectrum for suprathermal particles assumes a functional form that is extremely common (Gloeckler & Fisk 2006, 2010; Fisk & Gloeckler 2006, 2008; Fisk et al. 2010) with a power-law index γ_s for the distribution function $f \propto v^{\gamma_s}$ as a function of particle speed v (hereafter referred to as the common particle speed distribution, or common spectrum). This form applies at relatively low energies from ~3 keV up to ~160 keV (Fisk & Gloeckler 2012). The distribution function power-law index assumes a value, on average, that is close to −5 corresponding to a spectral index of $\gamma_s/2 + 1 = -1.5$ for the differential flux J as a function of energy E, $J \propto E^{\gamma_s/2+1}$. While this spectral form is common, Dayeh et al. (2017) found variations in the spectra for heavy ion species.

The presence of a common power law index poses a puzzle concerning the origin of suprathermal tails. Suprathermal tails observed by Ulysses typically at ~2–5 au are correlated with the levels of magnitude fluctuations in the heliospheric magnetic fields near SIRs (Schwadron et al. 1996). This correlation was attributed to the presence of magnetosonic waves that are transit-time damped during the acceleration of suprathermal ions. Fisk and Gloeckler proposed a specific acceleration mechanism that creates a v^{-5} distribution (Fisk & Gloeckler 2006, 2008, 2014). The mechanism is driven by local compressive turbulence and operates much like a magnetic pump. The common form of the spectrum could also result from acceleration processes that are stochastically distributed. In this case, the observed energy spectrum is a superposition of distributions from variable acceleration processes (Schwadron et al. 2010) including diffusive acceleration and statistical acceleration. Further, the common spectrum is so hard that it is close to the limit of possible stationary state plasma distributions out of equilibrium (Livadiotis & McComas 2009, 2010). It is possible that rapid acceleration processes driven by local compressive turbulence push the distribution close to this limit of stationary states out of equilibrium.

Suprathermal He^+ is produced from pickup ions (Moebius et al. 1985). These ions are predominantly photoionized from neutral He atoms that enter the heliosphere from the interstellar medium (Moebius et al. 1985; Schwadron 1998; Gloeckler & Geiss 1998, 2001). The source of interstellar pickup ions is well known, and modeled distributions based on the source reproduce observed distributions (e.g., Schwadron 1998; Schwadron et al. 1999). Despite the lack of variability in pickup ion production, the variable He^+ suprathermal tail index and the flux (Hill et al. 2009; Möbius et al. 2019; Popecki et al. 2013; Tessein et al. 2013; Taut et al. 2018) suggest that the tails are created by stochastically distributed processes including shocks, compressions and turbulence (Schwadron et al. 2010). Particles are accelerated by discrete sources, and then transported throughout the solar wind. Bower et al. (2020) present support for this concept using superposed epoch analyses of He^+ data from the PLASTIC instrument on STEREO-A at predominantly SIR shocks at 1 au. The tail index and suprathermal flux vary systematically across the shock. The observed power-law index agrees with the prediction of diffusive acceleration based on the compression ratio at the shock. Statistical analysis of suprathermal PUI power-law slopes in shocks with widely varying compression strengths showed that values close to −5 were the most common.

Two takeaways on the formation of the energy spectrum observed in the inner heliosphere are as follows: first, despite the variability in acceleration mechanisms and in underlying distributions, the average functional dependence on speed for accelerated suprathermal tails is observed to attain a relatively common form with

$$f_s(v) \propto v^{\gamma_s} \exp(-v/v_s), \tag{1}$$

where $\gamma_s \approx -5$ and $v_s \sim 4400$ km s^{-1} is the particle speed at ~10× the solar wind speed or, equivalently, ~0.16 MeV. The exponential roll-over at higher suprathermal energies is directly observed by the ULEIS instrument on ACE (Fisk & Gloeckler 2012). Second, there are various acceleration mechanisms associated with suprathermal tails, and strong advocates for each of them. While the underlying physical mechanism that explains these suprathermal tails is an area of active research, there is an increasing number of studies concluding that the average spectrum within SIRs attains a common form (Eq. (1)). This result is used in this paper to characterize the energetic particle spectrum near SIR compressions and shocks.

The recent observations of energetic particles from SIRs by PSP IS⊙IS (McComas et al. 2019; Desai et al. 2020; Cohen et al. 2020; Joyce et al. 2021; Allen et al. 2020a) provide some unique features. The vantage point of PSP close to the Sun allows the spacecraft to observe magnetic field lines spanning an enormous range of the inner heliosphere. Here, we discuss the profiles of energetic particles observed by IS⊙IS following the passage of a stream interaction region to discern both the magnetic structure within the rarefaction region that trails the CIRs, and the nature of particle acceleration from these structures.

This paper is a companion to the work of Joyce et al. (2021), which analyzes the SIR energetic particles observed day-of-year 320–325 in 2018 (November–21). In the inner heliosphere, typically at or inside 1 au, lower energy particles below ~1 MeV/nuc are expected to show the signatures of modulation with reduced lower energy fluxes and hardened energy spectra due to inhibited propagation of ions that are scattered as they move many au from the SIR reverse compression or shock to the point of observation. However, Joyce et al. (2021) find little or no evidence of modulation of lower energy particles. The relative lack of modulation is also found by Allen et al. (2020a) in PSP IS⊙IS and STEREO A observations of a CIR event from DOY 258–273 in 2019 (September 15–30). Our paper examines how this reduced modulation can be accounted for, and how the rapid evolution of energetic particle fluxes from SIRs can be explained. This paper offers an explanation for these fundamental questions and therefore develops a new view of energetic particles from stream interactions regions.

The paper proceeds by first discussing the observations of SIR time-profiles in Sect. 2 and the revision to the magnetic structure needed to explain observed time-profiles in Sect. 3. We discuss the energetic particle spectrum at SIRs in Sect. 4. We explore the implications of our findings in Sect. 5 and conclude in Sect. 6. There are five appendices in the paper that detail the sub-Parker spiral Appendix A, the distance to the SIR compression or shock Appendix B, the injection energy into diffusive shock acceleration Appendix C, the cooling rates of SIR suprathermal populations Appendix D, and the modeling of energetic particle propagation in to the position of PSP Appendix E.

2. IS⊙IS observations of energetic particles from SIRs

Parker Solar Probe's vantage point close to the Sun provides a unique platform to observe the progression of CIR acceleration throughout the inner heliosphere. Figure 1 shows a summary of the observations from IS⊙IS on day 318 through 325 of 2018. The passage of the stream interface occurs near the end of day 318. During passage of the stream interface, there is a small enhancement in the EPI-Lo count rate, which possibly indicates local particle acceleration (Allen et al. 2020b), and after the passage of the stream interface, we observe the gradual build-up and subsequent decay of particle fluxes where magnetic field lines are connected to the SIR compression and shock that forms further out in the heliosphere.

The average integrated flux is computed from the differential flux for each bin multiplied by the width of the energy bin, then summed and divided by the total of the energy bin widths. The EPI-Hi data is comprised of all protons, and the EPI-Lo fluxes are proton-dominated, but also include small contributions from other species. The EPI-Hi fluxes are from the A and B sides of LET1, which are sunward and anti-sunward facing, respectively (A_ and B_H_Flux from psp_isois-epihi_l2-let1-rates3600). The fluxes are summed over energy bins spanning 1.00-5.66 MeV. The data is binned hourly and then smoothed (boxcar averaged) over 5 h intervals.

The EPI-Lo fluxes are Ion TOF-only (H_Flux_ChanT from psp_isois-epilo_l2-ic). They are averaged over the three anti-sunward-facing wedges (W0, W6 and W7; apertures,0-9 and 60-79) and summed over energy bins spanning 166.47–496.27 keV. The data are binned hourly and smoothed over 11 h intervals.

The average sunward directed fluxes (red curves) and anti-sunward fluxes (blue curves) are shown in Fig. 1, panels 1 and 3. The observations indicate weak anisotropies, consistent with a distant source from the SIRs.

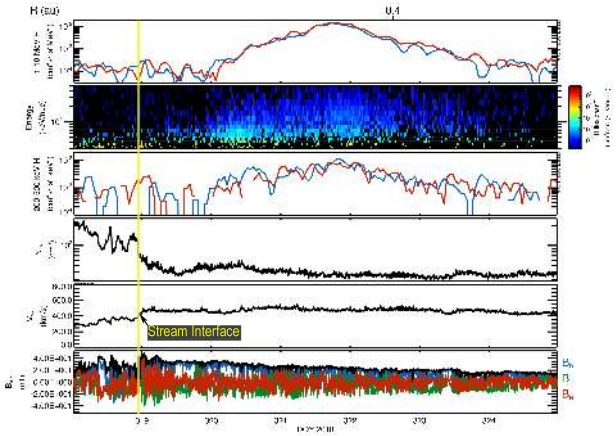

Fig. 1. Summary of energetic particles following the stream interaction region: (*top*) EPI-Hi proton fluxes (sunward directed particles in blue, anti-sunward particles in red) from 1–10 MeV, (*panel 2*) EPI-Lo proton fluxes as a function of energy and time, (*panel 3*) EPI-Lo proton fluxes as a function as a function of time from 200–500 keV, (*panel 4*) density measured by SWEAP, (*panel 5*) solar wind speed measured by SWEAP, and (*panel 6*) magnetic field measured by FIELDS. This figure is similar to Fig. 2 of Joyce et al. (2021); the only difference is in *panel 3*, which is shown from 100–500 keV H^+ in Joyce et al. (2021).

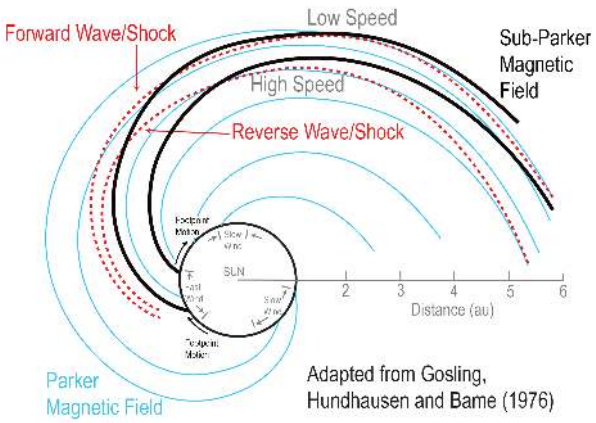

Fig. 2. Illustration of the magnetic field structure in a stream interaction region (SIR) adapted from Gosling et al. (1976). Within SIRs, Faster solar wind overtakes slower solar wind, forming a compression or shock (red dashed curves). The Parker Spiral magnetic field lines are shown as thin blue curves. With footpoint motion at the Sun, magnetic field lines (black curves) are connected between fast and slow solar wind and form the sub-Parker spiral (Murphy et al. 2002; Schwadron & McComas 2005; Schwadron et al. 2005) in rarefaction regions where the fast solar wind stretches out magnetic field lines in the radial direction.

3. Magnetic field structure of the rarefaction region behind the SIR

The magnetic field structure within the rarefaction region behind the SIR is taken traditionally to be a Parker Spiral. However, numerous studies have shown the magnetic field structure within the solar wind conforms to a sub-Parker spiral (Murphy et al. 2002; Schwadron 2002; Schwadron & McComas 2005; Schwadron et al. 2005). Footpoint motion at the Sun associated with differential rotation (Fisk 1996; Fisk et al. 1999) and interchange reconnection (Fisk & Schwadron 2001) create the condition where magnetic field lines are connected across the source regions of slow and fast solar wind. This results in magnetic field lines that are dragged out more quickly in the fast solar wind, creating a magnetic field structure in the inner heliosphere with a radial component significantly larger than that of a Parker Spiral magnetic field. The deviations in field direction are extremely prominent and commonly observed by Ulysses in corotating rarefaction regions (Murphy et al. 2002; Schwadron & McComas 2005; Schwadron et al. 2005). The magnetic field structure is illustrated in Fig. 2 (black field lines).

Appendix A describes the sub-Parker magnetic field structure, and Appendix B derives the distance along magnetic field lines to the compression or shock. Figure 3 shows the distance to the SIR compression or shock along the magnetic field (top panel), and the distance to the SIR in the radial direction (second panel). The sub-Parker spiral (black curves) due to its larger radial component than the Parker Spiral (blue curves) provides a

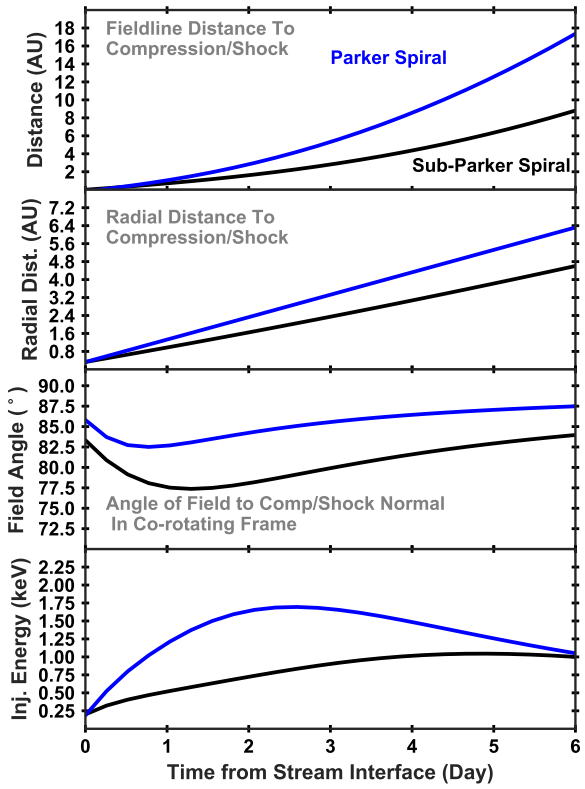

Fig. 3. Distance along the sub-Parker spiral (black curves) is shorter than along the Parker Spiral (blue curves) to Stream Interaction Regions, and a the sub-Parker magnetic field is associated with a lower injection energy compared to a Parker field. We show (*top panel*) the distance along a magnetic field line to the SIR compression or shock, and (*second panel*) the radial distance to the SIR compression/shock. These distances are shown as a function of time from stream interfaces at $r_o \sim 0.33$ au where the observations are made by IS⊙IS. The sub-Parker spiral also causes a reduced angle (*third panel*) between the magnetic field and the normal to the SIR compression or shock. Note that the field-to-normal angle at the SIR compression or shock is calculated in the corotating reference frame. The injection energy detailed in Appendix C is also shown (*fourth panel*).

more direct connection through the rarefaction region to the SIR. The parameters associated with footpoint motion are taken from Schwadron (2002) and detailed in Appendices A and B.

The shorter connection to the site of acceleration for a sub-Parker field configuration is evident in Fig. 3. Both the distance along the field to the SIR reverse compression or shock and the radial distance to this location are reduced along a sub-Parker spiral.

The sub-Parker magnetic structure also reduces the angle between the magnetic field and the normal of the shock or compression, and the injection energy into diffusive acceleration. Note that this field angle is reported in the corotating reference frame, a natural choice for treating particle acceleration associated with SIR Ions. Ions require a sufficient speed to be able to move upstream along the magnetic field relative to the shock or compression. This injection speed described in Appendix C is simply $v_{inj} = u_1/\cos\theta_1$ in the limit that particles are restricted to a magnetic flux tube. Here, u_1 is the upstream speed and θ_1 is the angle between the magnetic field and the normal to the shock or compression. This expression for the injection speed neglects cross-field diffusion and drift (associated with a small antisymmetric term in the diffusion tensor), but includes several of the key factors that control the injection speed. The inverse-cosine dependence indicates that ions must have higher speed to move upstream on field lines that make at large angles θ_1 to the shock or compression. Increased plasma speed upstream also increases the injection speed. The injection speed and energy are solved for including the effects of cross field diffusion (we take $\kappa_\perp/\kappa_\parallel = 0.01$) and drift as detailed in Eq. (C.5) from Giacalone (2001).

The low injection speed at the SIR enables diffusive acceleration across a large range of energies from pickup ion energies (several keV) up through the energetic particle energies at >1 MeV/nuc. The particle energy spectrum observed within SIRs attains, on average, a common function with a power-law for the distribution function close to v^{-5} and an exponential roll-over at ~0.16 MeV, as detailed previously. In the next section, we use this common form of the spectrum and the observations from IS⊙IS to infer the rate associated with acceleration energetic particles through the inner heliosphere.

4. The energetic particle spectrum at SIRs

We use IS⊙IS observations to determine energetic particle fluxes on magnetic field lines that connect to the acceleration region in SIRs. We consider particle acceleration at SIRs involving a two-step process (Schwadron et al. 1996). In the first step suprathermal ions are accelerated, and the second step is due to diffusive shock acceleration at the compression or shock. The first step of the acceleration process occurs at lower suprathermal energies, whereas the second step is responsible for accelerating particles to higher MeV energies. As discussed further in the next session, there is no sharp energy boundary separating these two steps.

Bower et al. (2020) showed that the energetic particle spectra at SIR shocks are consistent with diffusive shock acceleration. These authors conclude that averaging over sufficiently long periods leads to distribution functions with $f \propto v^{-5.4}$, close to the −5 power-laws discussed by Fisk and Gloeckler. This supports the conclusion that the roughly fixed spectral behavior, the common particle speed distribution, may be the result of the superposition of stochastically distributed processes including shocks, compressions and turbulence (Schwadron et al. 2010).

We use the common particle speed distribution to understand the rates associated with particle acceleration in the SIR. At the SIR compression and reverse shock, we take the functional form for the distribution function specified by Eq. (1) with $\gamma_s = -5.4$ and the roll-over begins at particle speed $v_s = 4400$ km s^{-1}. The question of how the common particle speed distribution is maintained is taken up in the next section.

In Appendix D, we show that with the common particle speed distribution and a fixed rate of particle acceleration ($\dot{a}_s$), the distribution function must increase exponentially with distance, as $\exp(\dot{a}_s r/u)$. Here u is average radial solar wind speed across the SIR and the rate associated with particle acceleration is related to the average divergence of flow within the SIR, and the rate of statistical acceleration (see Eq. (D.4)).

If instead of compression and statistical acceleration within the SIR, there is cooling due to solar wind expansion, the distribution function decreases with radius, as $r^{g\gamma_s/3}$ where g is the solar wind expansion factor (e.g., for radial expansion, $g = 2$). The time profiles of energetic particles from IS⊙IS constrain first the rate associated with suprathermal acceleration during the merging of faster wind with slower wind within the SIR, and then the rate associated with cooling at distances where the SIR breaks down.

The substantial rise in both higher energy and lower energy energetic particle fluxes is observed by IS⊙IS up to $\tau_{peak} \sim 3$ days after passage of the stream interface. For the sub-Parker spiral, the field lines observed near $\tau_{peak} \sim 3$ days connect out to a radial distance of ~2.6 au.

This 2.6 au distance is not a coincidence, as explained in the following paragraph. The SIR forms compressions and then shocks due to the merging of the fast wind into slower wind. Typically, this process occurs with a reverse wave or shock moving backward (upstream) into the faster wind, and a forward wave or shock moving ahead (downstream) into the slower wind. The breakdown of the SIR occurs at the point where either the forward wave merges through all of the slow wind in front of it, or the reverse wave moves through the faster wind behind the SIR. PSP Observations show that prior to the passage of the interface, the slower wind persists for $\tau_1 \sim 3$ days. This period of slower wind constitutes a change in longitude of $\Delta\phi_1 = \Omega_\odot \tau_1 = 41.5°$. We observe the faster stream with radial speed $V_h \sim 530$ km s^{-1}, whereas the slower stream moves with radial speed $V_1 \sim 320$ km s^{-1} and the intermediate speed wind within the SIR has radial speed $V_m = 425$ km s^{-1}. In the corotating frame these streams move outward along an Archimedian spiral. At a radial distance given by $r_{peak} = r_o + \tau_1 V_m V_1/(V_m - V_1) = 2.6$ au, the slower wind spiral on the forward interface intersects with the spiral associated with intermediate speed wind observed by PSP near the stream interface. In other words, it is at the radial distance of 2.6 au where the faster wind within the SIR sweeps up the majority of slower wind in front of the SIR. This corresponds to where IS⊙IS observes the peak in energetic particle fluxes from the SIR and suggests that the particle acceleration within the SIR persists while streams merge, and accordingly suprathermal fluxes increase. After streams within the SIR have merged, the compression of the SIR gives way to expansion, causing the suprathermal distribution to cool, and accordingly energetic particle fluxes to decrease.

We analytically solve for the distribution function at the SIR reverse compression and shock (Appendix D), and numerically model the propagation of energetic particles back to the location of PSP (Appendix E). Acceleration at the rate $\dot{a}_s$ explains the rising level of the suprathermal population out to radius r_{peak} while the faster solar wind continues to overtake slower wind within the SIR. Beyond r_{peak}, the distributions cool at a rate that is determined from the expansion of solar wind (D.6), which we parameterize according to the expansion factor g.

The propagation model solves for diffusion of energetic particles in the rarefaction region trailing the SIR. We solve for diffusion parallel and perpendicular to the magnetic field (Appendix E). The parallel diffusion coefficient is scaled with radial distance $\lambda_\parallel = \lambda_0 (r/r_1)^{1.3}$ (Erdos et al. 1999) and we take $\kappa_\perp/\kappa_\parallel = 0.01$ which is on the low end of the range generally considered by Giacalone & Jokipii (1999).

Results of the model are compared to observations in Fig. 4. The model uses a scattering mean free path of $\lambda_0 = 1$ au, a rate associated with particle acceleration $\dot{a}_s = 7.1 \times 10^{-6}$ s^{-1} (equivalent to a timescale for acceleration of ~1.6 days), an expansion factor of $g = 3.1$, and a peak injection efficiency of $\epsilon = 1/2$. The value of the rate associated with particles acceleration is chosen to account for the rise in fluxes over the first 3 days after passage of the stream interface, and the expansion factor is chosen to account for the subsequent fall in energetic particle fluxes. These results are discussed further in the next section where we show that the deduced rate associated with particle acceleration is consistent with a combination of compression within the SIR and statistical acceleration. Further, the expansion factor

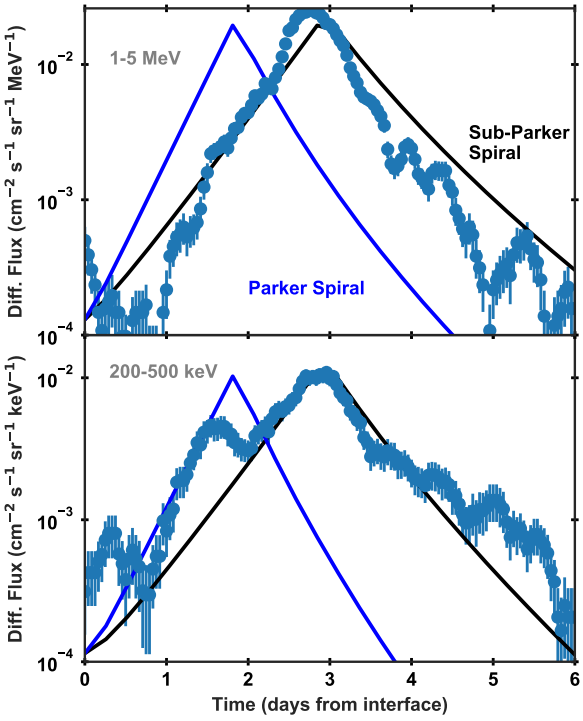

Fig. 4. Comparison between observed (blue data points) and modeled (curves) differential fluxes at higher and lower energies. Modeled energetic particles are accelerated at the SIR reverse compression or shock and propagate back to PSP along sub-Parker field lines (black curves) and Parker field lines (blue curves). Observed differential fluxes (averaged over 1–5 MeV, *top*, and 200–500 keV, *bottom*) are compared with modeled fluxes (2 MeV, *top*, and 250 keV, *bottom*).

is consistent with weak super-radial expansion driven by the SIR over-pressure that occurs after the streams have merged within the SIR.

The long scattering mean free path is needed to account for the similar time evolution of lower energy and higher energy fluxes. With a much shorter scattering mean free path, the ratio of the lower energy to higher energy fluxes would drop quickly after passage of the stream interface. Instead, we observe both lower energy (200–500 keV fluxes) and higher energy (1–5 MeV) fluxes to persist many days after the passage of the stream interface. This indicates that both the lower and higher energy fluxes are weakly modulated by the solar wind.

Another indication of the weak modulation is found by examining the slopes in the modeled distributions (Fig. 5). Note that the power-law indexes are relatively stable functions of time past the stream interface. The observations early in the event (the first day) show steeper power-laws, and afterward the power-laws are observed to become fairly stable with time (Joyce et al. 2021), in agreement with the simulation. Strong modulation causes an increase in the power-law index, and a hardening of spectrum particularly at lower energies. The long scattering mean free path indicated here is also consistent with observations of pickup ions from Ulysses/SWICS that showed large anisotropies (e.g., Gloeckler et al. 1995; Isenberg 1997; Schwadron 1998).

Several important differences are observed between observations and simulations. First, the spectral index of the 1–5 MeV differential fluxes are generally in the range of −5 to −6 (corresponding to power-law indexes in the distribution function of −12 to −13), whereas simulations show differential flux power-laws of approximately −4 (corresponding to a power-law index

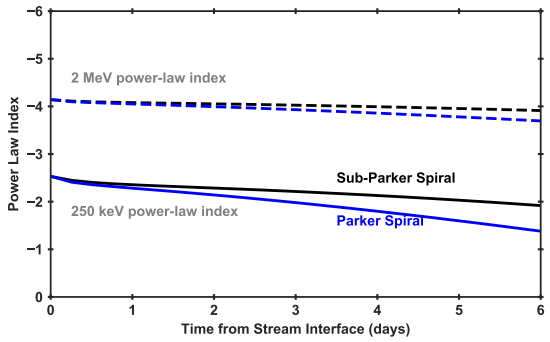

Fig. 5. Spectral index s of the modeled differential fluxes as a function of time after passage of the stream interface. Power-law indexes γ_s for the distribution correspond to $\gamma_s = 2(s-1)$. For example, a spectral index of $s = -2$ corresponds to a power-law index of $\gamma_s = -6$, which is close to the −5.4 power-law used for the common particle speed distribution.

for the distribution function of −10). We discuss this difference further in the next section as a possible indication of broken power-law distributions from SIRs, as opposed to the exponential roll-over used in our empirical form for the speed distribution. Second, as already mentioned, the spectral indices during the first day in the lower energy range are observed to be approximatly −3 (Joyce et al. 2021) (power-law index −8) whereas simulations show spectral indexes for the differential flux of approximately −2.5 (power-law index −7) near 250 keV. This suggests that early in the SIR acceleration process, suprathermal distributions are slightly softer than later in the acceleration process when the SIR compression has formed fully into a shock.

In the next section, we further discuss the implications of IS⊙IS observations pertaining to both the magnetic field structure within the rarefaction region, and the processes responsible for suprathermal particle acceleration.

5. Discussion

5.1. Magnetic field structure and footpoint motion

The magnetic structure of the rarefaction region shows much more direct connection to the SIR for the sub-Parker spiral. This is essential in explaining the long period of time (6 days) when energetic particle enhancements are observed after passage of the stream interface. Further, the Parker Spiral field lines quickly connect out to large distances in the heliosphere, and, as a result the emission from the SIR is expected to peak in less than 2 days following passage of the stream interface.

The sub-Parker spiral (Murphy et al. 2002; Schwadron 2002; Schwadron & McComas 2005; Schwadron et al. 2005) confirms that footpoint motion at the Sun associated provides a magnetic fieldline connection between regions of fast and slower solar wind. The resulting large-scale magnetic configuration (see Fig. 2) provides access for energetic particles throughout the inner heliosphere. The IS⊙IS observations at PSP provide further validation for this large-scale magnetic field structure.

An important question at this stage is how common the sub-Parker field structure is. The sub-Parker spiral appears to be observed in almost all rarefaction regions studied by Ulysses, but there has not yet been a systematic study that attempts to determine how frequently the sub-Parker magnetic structure is present. It is interesting in Fig. 4 that variations in the time evolution suggest the presence of magnetic flux tube that may have variable large-scale structure. For example, in the period between day 1 and 2 past the stream interface, there appears to be a structure that conforms more closely to the Parker Spiral, at least at lower energies. Since footpoint motion is driven in part by interchange reconnection, it is likely that footpoint motion is itself nonuniform. Nonuniformity in footpoint motion should lead to variations in the magnetic fieldline connection across regions of faster and slower solar wind source regions. From source regions where footpoint motion is restricted, we would expect the large-scale magnetic structure to conform more closely to a Parker Spiral, whereas regions with faster footpoint motion would conform to the sub-Parker spiral.

This discussion reveals that IS⊙IS observations of SIRs may hold the key to understanding the variability of footpoint motion at the Sun, which remains a fundamental question linked to the source of solar wind and the global structure of the corona (Fisk 1996; Fisk et al. 1999; Schwadron et al. 1999; Fisk & Schwadron 2001; Schwadron & McComas 2003a) and energetic particle propagation through the heliosphere (Schwadron & McComas 2003b). Therefore, systematic study of IS⊙IS observations from SIRs would help us understand the large-scale structure of heliospheric magnetic field, its link to the source of the solar wind and the sources of energetic particle variability within the heliosphere.

5.2. Suprathermal particle acceleration

The rapid rise in fluxes observed by IS⊙IS in the buildup to the intensity peak is associated with acceleration of the suprathermal population within the SIR. From the observations, we derive a rate associated with particle acceleration $\dot{a}_s = 7.1 \times 10^{-6}$ s^{-1}. In Appendix D, we relate this rate to compression and statistical acceleration, Eq. (D.4). Observations from Ulysses show the buildup of density (n_s) within SIRs in the range of $n_s/n_0 = 10$–15 times that (n_0) in the ambient surrounding solar wind (Crooker et al. 1999). Because of mass conservation, this buildup in density is used to determine the average compression within the SIR:

$$\begin{aligned}\dot{a}_s^{\rm comp} &= \gamma_s \langle \nabla \cdot \boldsymbol{u} \rangle_s / 3 \\ &= (-\gamma_s/3) u_s \ln(n_s/n_0)/r. \end{aligned} \quad (2)$$

Here, $\langle \nabla \cdot \boldsymbol{u} \rangle_s = -u_s \ln(n_s/n_0)/r$ is the divergence of the bulk flow velocity within the SIR, u_s is the flow speed within the SIR, and $r \approx 2.6$ au is the distance up to the density peak. With these quantities, we find $\dot{a}_s^{\rm comp}$ in the range 4.5×10^{-6} to 5.3×10^{-6} s^{-1}, which is ∼65−75% of the rate of acceleration needed to explain the buildup in the suprathermal flux.

Statistical acceleration through wave-particle interactions also contributes to the rate of suprathermal acceleration. For example, transit-time damping of magnitude fluctuations in the magnetic field is a known source of rapid particle acceleration (Schwadron et al. 1996). Rates associated statistical acceleration were determined from Ulysses/SWICS observations both from observed fluctuations in the magnetic field and from the tails of suprathermal distribution functions. Rates for second-order velocity-space diffusion were found to range from $D_{pp}/p^2 \sim 2 \times 10^{-7}$ to 8×10^{-7} s^{-1} at ∼3 times the solar wind speed. As discussed in Appendix D, this second–order diffusion contributes to the acceleration at rate $\dot{a}_s^{\rm stat} \approx \gamma_s^2 D_{pp}/p^2 \approx 5.8 \times 10^{-6}$ s^{-1} to 2.3×10^{-5} s^{-1}, which is 80–330% of the needed rate associated with particle acceleration. Both compression and statistical acceleration in SIRs contribute to the acceleration of suprathermal protons. Further, processes involving second-order statistical

acceleration appear likely to contribute the majority of the needed rate associated suprathermal acceleration.

The two-step acceleration process within SIRs requires some additional explanation to account for observations. If ions were first statistically accelerated and then injected into diffusive acceleration, there would be a clear break in the energy spectrum between the ions with energies below the injection energy and higher energy particles involved in diffusive acceleration at the SIR shock or compression. The fact that no break is observed is an indication that the two-step acceleration process does not have a clear boundary between lower energy suprathermal ions and higher energy particles that are diffusively accelerated. Simulations by Chen et al. (2015) confirm this point. Within SIRs there is a clear power-law from suprathermal energies up to ~150 keV, which is likely the result of multiple processes contributing to the acceleration of the suprathermal ions that are injected into diffusive acceleration.

Removing the first step of the acceleration process also poses problems. If we remove the first step, the diffusively accelerated power-laws should not build up increasing fluxes with distance through the inner heliosphere. In this case, we would expect a power-law from the injection energy, and a roll-over or a broken power-law (Schwadron et al. 2015a,b) to higher energies. However, IS⊙IS data show the build up of suprathermal fluxes up to the peak fluxes (Fig. 4), indicating that the first step of suprathermal acceleration must be occurring.

It is likely that both suprathermal particle acceleration via wave-particle interactions and compression build up fluxes within the SIR. STEREO-A/PLASTIC observations directly show the compression and compressive turbulence that increase the pickup ion cutoff energy in SIRs (Bower et al. 2019). As the compression regions bounding the SIR form into shocks, suprathermal ions that form power-law tails participate in both first-order acceleration at the shock or compression, and second-order acceleration and compressive acceleration inside the SIR. This explains both the maintenance of the power-law from diffusive acceleration and the build-up of fluxes from compressive acceleration and statistical acceleration inside or near the SIR. The observed power-law is therefore a superposition of the contributions to suprathermal acceleration from compressions, shocks, and turbulence (Schwadron et al. 2010). This implies that the observed power-law is not a singular reflection of any individually observed compression ratio, and the superposition process maintains greater stability in the observed power-law.

Our discussion of suprathermal acceleration up to this point appears to neglect the specific acceleration process that Fisk and Gloeckler argue acts to form observed power-law tails (Fisk & Gloeckler 2006, 2008, 2014). However, the averaging implicit to the superposition conjecture (Schwadron et al. 2010) reproduces features associated with a variety of different acceleration mechanisms. For example, Fisk et al. (2010) consider three possible approaches for explaining the common spectral form: (1) the acceleration mechanism of Fisk and Gloeckler in which energy is redistributed from a core particle population into the suprathermal tail; (2) traditional stochastic acceleration in which particles are accelerated by damping turbulence; and (3) the statistical approach introduced by Schwadron et al. (2010) in which the −5 spectrum is formed by averaging over individual spectra. The study (Fisk et al. 2010) concludes that the statistical approach of Schwadron et al. can yield the −5 spectrum and is consistent with the results of Fisk and Gloeckler when the distribution functions for individual events and the averaging technique are compatible. The superposition conjecture can reproduce observations under a wide variety of types of underlying variability. Bower et al. (2020) find significant levels of variability within the observations, and yet reveal the common spectrum when averaging over this variability. The emergence of the common spectrum after averaging out variability provides direct support for the superposition conjecture. Corroborating this further for the event shown in Fig. 1, we note that the event has an average spectral index of −2 (corresponding to a distribution function $f \propto v^{-6}$ velocity spectrum) (Joyce et al. 2021), which is similar to the index of −1.75 (corresponding to $f \propto v^{-5.5}$ velocity spectrum) found by Bower et al. (2020).

It is notable that the early acceleration within the SIR (observed ~1−2 days after the stream interface passage) does not form the common particle energy spectrum. Over this period, Joyce et al. (2021) show a markedly softer spectrum in low energy fluxes. This trend can also be observed in Fig. 1 on DOY 320 where we observe an excess of 40 keV protons. This reflects the early development of the energy spectrum that hardens as the SIR compression moves beyond 1–1.5 au and begins to form into a more defined structure or a shock.

The emergence of a common spectrum from SIRs and CIRs requires that the acceleration process operate in a region where turbulence, compression and possibly shocks cause the build-up of the suprathermal particle population. The compression regions of SIRs and CIRs develop where faster solar wind streams overtake slower streams. It is here where the development of compressional acceleration, compressive waves and turbulence, and transit-time damping (Schwadron et al. 1996) take place naturally. After the compression has developed fully, typically around or beyond 2.5 au, the compressions bounding SIRs and CIRs may also form into shocks. However, the development of shocks is not a necessary precursor for particle acceleration, and in many small SIRs, the faster and slower streams may merge prior to the development of a shock. We emphasize these points to avoid confusion about the development of the common spectrum: the suprathermal acceleration process occurs within or near the SIR or CIR compressed or shocked plasma, and energetic particles are transported from the sites of acceleration back to the location of PSP. As a result of the sub-Parker spiral magnetic field, energetic particles are transported more readily from the SIR or CIR through the rarefaction region. However, it is very unlikely that significant acceleration occurs within the rarefaction region.

Starting ~3 days after passage of the stream interface, we observe a sharp decline in energetic particle fluxes (Fig. 4), which is readily explained by the expansion of the remnants of the SIR after the fast wind has overtaken the slower wind (beyond 2.6 au). The drop in fluxes is so rapid that we inferred an expansion factor of $g \approx 3$, corresponding with super-radial expansion. This over-expansion could be the result of the over-pressure in the plasma and suprathermal ions that has built up from SIR compressions.

While this discussion has focused on H^+, the observed trends in energetic He ions are also consistent with ease of inward transport from the sites of acceleration into the location of PSP at ~0.33 au. In commenting on the same event reported here, but in the context of He ions, Desai et al. (2020) state: “the spectrum flattens but does not turn over as expected from energy losses due to adiabatic deceleration during transport from an SIR shock located well beyond 1 au”. In other words, the low-energy spectrum of He also indicates the lack of modulation, and the ease of inward transport of He ions.

Desai et al. (2020) go on to describe observations of He ions in terms of “magnetic channels” invoked by McDonald & Burlaga (1985) to explain how SEPs accelerated near the Sun

and Jovian electrons can propagate to Earth orbit (Mewaldt et al. 1976; Chenette 1980; Roelof et al. 1996). This magnetic channeling is likely a natural result of the more direct radial access provided by the sub-Parker spiral magnetic field.

5.3. Higher energy particle acceleration in SIRs

The energetic particle fluxes at lower and higher energies (Fig. 4) track each other remarkably well. Notably, the excess of lower energy fluxes and the deficit at higher energies between day 1 and 2 past the interface is consistent with the acceleration process beginning at lower energies and extending to higher energies progressively as a function of distance and therefore time within or near the SIR. The power-law index determined from simulations (Fig. 5) is harder than observed at these higher energies (1–5 MeV), the energy spectrum appears to be a broken power-law (Joyce et al. 2021), and the higher energy spectral index is approximately −5.1 (Cohen et al. 2020; Joyce et al. 2021).

The broken power-law distribution is commonly observed in large solar energetic particle events (Mewaldt et al. 2012). One explanation is that these broken power-laws (Schwadron et al. 2015b) are associated with CME expansion regions low in the corona that are effective accelerators over a finite spatial region. There is a rigidity regime where particles effectively diffuse away and escape from the acceleration sites that leads to the formation of broken power-law distributions. An extension of this idea is that SIR compressions and shocks also have a regime of high rigidity (and high energy) ions that diffuse away and escape the acceleration region to form broken power-laws.

6. Summary and conclusions

We have examined the distributions observed by IS⊙IS when PSP was near 0.33 au following the passage of a stream interface on DOY 318–325 in 2018. Details concerning the energetic particle distributions are published in a companion paper (Joyce et al. 2021). We model distributions at the SIR compression and shock based on a common form of the particle energy distribution observed throughout the inner heliosphere (Gloeckler & Fisk 2006, 2010; Fisk & Gloeckler 2006, 2008; Fisk et al. 2010; Bower et al. 2020). We compare the results of a propagation model using a Parker field and a sub-Parker Magnetic field configuration.

Observations extending from ~30 keV up to ~5 MeV show energetic particle flux enhancements for roughly a week past the stream interface. Five days after passage of the stream interface, a standard Parker field configuration has field lines that extend from PSP over distances of more than 12 au to the SIR. These large distances along the Parker Spiral field lines make it difficult to understand how enhancements in fluxes can be observed at PSP so long after the passage of the stream interface, particularly at low energies.

The sub-Parker magnetic field configuration provides a much shorter connection to the SIR, and explains why IS⊙IS observes energetic particle enhancements long after the stream interface passage. The magnetic field configuration arises due to footpoint motions at the Sun driven by differential rotation and interchange reconnection. The energetic particle evolution observed by IS⊙IS provides evidence that footpoint motion at the Sun structures the magnetic field throughout the inner heliosphere.

The rapid rise in energetic particle fluxes observed before day 3 after the passage of the stream interface indicates acceleration of suprathermal particles associated both with compression within the SIR and statistical acceleration. The interplay between the acceleration of suprathermal ions in the SIR and diffusive shock acceleration to >MeV energies explains the development of the common particle energy spectrum and the rapid rise in energetic particle fluxes.

For the period following day 3 after the passage of the stream interface, energetic particle fluxes rapidly decrease, reflecting the sub-Parker fieldline connection to the SIR as it decays. During this period, the sub-Parker field lines connect to the SIR at radial distances beyond 2.6 au where the faster wind has fully overtaken the slower solar wind in front of it. The cooling of energetic particle distributions at distances beyond 2.6 au are consistent with over-expansion of the solar wind in this region driven by the overpressure of the plasma and suprathermal ions within the SIR.

This paper develops a methodology to analyze the observations by IS⊙IS on PSP associated with Stream Interaction Regions. The new vantage point from PSP close to the Sun enables observation of the energetic particle fluxes from the Stream Interaction Region as it develops and then decays further out in the heliosphere. Suprathermal acceleration is critical in explaining the evolution energetic particle fluxes from the Stream Interaction Region. The evolution of energetic particles from the Stream Interaction Region provides a unique way to probe the global magnetic structure of the inner heliosphere. Thus, the new view of Stream Interaction Regions observed by IS⊙IS on Parker Solar Probe provides evidence of the deviation from the standard Parker Spiral in rarefaction regions in the inner heliosphere, and the rate associated with suprathermal particle acceleration within Stream Interaction Regions.

Acknowledgements. We are deeply indebted to everyone that helped make the Parker Solar Probe (PSP) mission possible. We thank all of the outstanding scientists, engineers, technicians, and administrative support people across all of the IS⊙IS, FIELDS and SWEAP institutions that produced and supported the IS⊙IS, FIELDS and SWEAP instrument suites, support its operations and the scientific analysis of its data. This work was supported as part of the PSP mission under contract NNN06AA01C. NAS and CMSC were also supported under LWS grant "New Insights into SEP Sources, Acceleration, and Propagation: an Integrated Observation-Modeling Approach", grant number 80NSSC19K0067. The IS⊙IS data and visualization tools are available to the community at: `https://spacephysics.princeton.edu/missions-instruments/isois`; data are also available via the NASA Space Physics Data Facility (`https://spdf.gsfc.nasa.gov/`). Parker Solar Probe was designed, built, and is now operated by the Johns Hopkins Applied Physics Laboratory as part of NASA's Living with a Star (LWS) program (contract NNN06AA01C). Support from the LWS management and technical team has played a critical role in the success of the Parker Solar Probe mission.

References

Allen, R. C., Ho, G. C., Mason, G. M., et al. 2020a, Geophys. Res. Lett., 48, e91376
Allen, R. C., Lario, D., Odstrcil, D., et al. 2020b, ApJS, 246, 36
Bale, S. D., Goetz, K., Harvey, P. R., et al. 2016, Space Sci. Rev., 204, 49
Barnes, C. W., & Simpson, J. A. 1976, ApJ, 210, L91
Bower, J. S., Möbius, E., Aly, A., et al. 2020, J. Phys. Conf. Ser., submitted
Bower, J. S., Moebius, E., Berger, L., et al. 2019, J. Geophys. Res. Space Phys., 124, 6418
Chen, J. H., Schwadron, N. A., Möbius, E., & Gorby, M. 2015, J. Geophys. Res. Space Phys., 120, 9269
Chenette, D. 1980, J. Geophys. Res. Space Phys., 85, 2243
Chotoo, K., Schwadron, N. A., Mason, G. M., et al. 2000, J. Geophys. Res., 105, 23107
Cohen, C. M. S., Christian, E. R., Cummings, A. C., et al. 2020, ApJS, 246, 20
Crooker, N. U., Gosling, J. T., Bothmer, V., et al. 1999, Space Sci. Rev., 89, 179
Dayeh, M. A., Desai, M. I., Mason, G. M., Ebert, R. W., & Farahat, A. 2017, ApJ, 835, 155
Desai, M. I., Mitchell, D. G., Szalay, J. R., et al. 2020, ApJS, 246, 56

Erdos, G., Balogh, A., & Jota, J. 1999, Int. Cosmic Ray Conf., 6, 316
Fisk, L. A. 1976, J. Geophys. Res., 81, 4633
Fisk, L. A. 1996, J. Geophys. Res., 101, 15547
Fisk, L. A., & Gloeckler, G. 2006, ApJ, 640, L79
Fisk, L. A., & Gloeckler, G. 2008, ApJ, 686, 1466
Fisk, L. A., & Gloeckler, G. 2012, Space Sci. Rev., 173, 433
Fisk, L. A., & Gloeckler, G. 2014, J. Geophys. Res. Space Phys., 119, 8733
Fisk, L. A., & Lee, M. 1980, ApJ, 237, 620
Fisk, L. A., & Schwadron, N. A. 2001, ApJ, 560, 425
Fisk, L. A., Zurbuchen, T. H., & Schwadron, N. A. 1999, ApJ, 521, 868
Fisk, L. A., Gloeckler, G., & Schwadron, N. A. 2010, ApJ, 720, 533
Fox, N. J., Velli, M. C., Bale, S. D., et al. 2016, Space Sci. Rev., 204, 7
Giacalone, J. 2001, in The Outer Heliosphere: The Next Frontiers (Amsterdam: Elsevier), 377
Giacalone, J., & Jokipii, J. R. 1999, ApJ, 520, 204
Giacalone, J., Jokipii, J. R., & Kóta, J. 2002, ApJ, 573, 845
Gloeckler, G., & Fisk, L. A. 2006, ApJ, 648, L63
Gloeckler, G., & Fisk, L. A. 2010, AIP Conf. Ser., 1302, 110
Gloeckler, G., & Geiss, J. 1998, Space Sci. Rev., 86, 127
Gloeckler, G., & Geiss, J. 2001, Space Sci. Rev., 97, 169
Gloeckler, G., Schwadron, N. A., Fisk, L. A., & Geiss, J. 1995, Geophys. Res. Lett., 22, 2665
Gosling, J. T., Hundhausen, A. J., & Bame, S. J. 1976, J. Geophys. Res., 81, 2111
Hill, M. E., Schwadron, N. A., Hamilton, D. C., Di Fabio, R. D., & Squier, R. K. 2009, ApJ, 699, L26
Isenberg, P. A. 1997, J. Geophys. Res., 102, 4719
Joyce, C. J., McComas, D. J., Schwadron, N. A., et al. 2021, A&A, 650, L5 (PSP SI)
Kasper, J. C., Abiad, R., Austin, G., et al. 2016, Space Sci. Rev., 204, 131
Livadiotis, G., & McComas, D. J. 2009, J. Geophys. Res. Space Physics, 114, 11105
Livadiotis, G., & McComas, D. J. 2010, ApJ, 714, 971
Mason, G. M. 2000, AIP Conf. Ser., 528, 234
McComas, D. J., Alexander, N., Angold, N., et al. 2016, Space Sci. Rev., 204, 187
McComas, D. J., Christian, E. R., Cohen, C. M. S., et al. 2019, Nature, 576, 223
McDonald, F. B., & Burlaga, L. F. 1985, Int. Cosmic Ray Conf., 4, 346
McDonald, F. B., Teegarten, B. J., Trainor, J. H., von Rosenvinge, T. T., & Webber, W. R. 1976, ApJ, 203, L149
Mewaldt, R. A., Stone, E. C., & Vogt, R. E. 1976, J. Geophys. Res., 81, 2397
Mewaldt, R. A., Looper, M. D., Cohen, C. M. S., et al. 2012, Space Sci. Rev., 171, 97
Möbius, E., Bower, J., Aly, A., et al. 2019, J. Phys. Conf. Ser., 1332, 012011
Moebius, E., Hovestadt, D., Klecker, B., Scholer, M., & Gloeckler, G. 1985, Nature, 318, 426
Murphy, N., Smith, E. J., & Schwadron, N. A. 2002, Geophys. Res. Lett., 29, 23
Popecki, M. A., Klecker, B., Simunac, K. D. C., Galvin, A. B., & Kucharek, H. 2013, AIP Conf. Proc., 1539, 255
Roelof, E. C., Simnett, G. M., & Tappin, S. J. 1996, A&A, 316, 481
Schwadron, N. A. 1998, J. Geophys. Res., 103, 20643
Schwadron, N. A. 2002, Geophys. Res. Lett., 29, 14
Schwadron, N. A., & McComas, D. J. 2003a, ApJ, 599, 1395
Schwadron, N. A., & McComas, D. J. 2003b, Adv. Space Res., 32
Schwadron, N. A., & McComas, D. J. 2005, Geophys. Res. Lett., 32, L03112
Schwadron, N. A., Fisk, L. A., & Gloeckler, G. 1996, Geophys. Res. Lett., 23, 2871
Schwadron, N. A., Fisk, L. A., & Zurbuchen, T. H. 1999, ApJ, 521, 859
Schwadron, N. A., McComas, D. J., Elliott, H. A., et al. 2005, J. Geophys. Res., 110, A04104
Schwadron, N. A., Dayeh, M. A., Desai, M., et al. 2010, ApJ, 713, 1386
Schwadron, N. A., Lee, M. A., Gorby, M., et al. 2015a, J. Phys. Conf. Ser., 642, 012025
Schwadron, N. A., Lee, M. A., Gorby, M., et al. 2015b, ApJ, 810, 97
Taut, A., Berger, L., Möbius, E., et al. 2018, A&A, 611, A61
Tessein, J. A., Matthaeus, W. H., Wan, M., et al. 2013, ApJ, 776, L8
Yu, J., Berger, L., Wimmer-Schweingruber, R., et al. 2017, A&A, 599, A13

Appendix A: The sub-Parker spiral

We follow the ballistic propagation of plasma parcels from the Sun within the solar wind to determine the structure of the magnetic field in the inner heliosphere. This calculation follows Schwadron (2002), and simplifies the formalism for application to energetic particle acceleration and propagation within CIRs. Figure A.1 shows the configuration near the Sun in the corotating reference frame along a boundary surface (at radius R_B) where footpoint motion moves magnetic footpoints between regions of faster wind (with speed $V + \delta V/2$) and regions of slower wind (with speed $V - \delta V/2$). The boundary surface is at a radius where the field has roughly reached a pressure balance (balance between magnetic pressure and ram pressure). Footpoints rotate in the azimuthal direction at rate $\omega_\phi = -|\omega_\phi|$ in the opposite direction of the Sun's rigid rotation (the rigid rotation rate is $\Omega_\odot$). Footpoints also move in colatitude at rate $\omega_\theta = |\omega_\theta|$.

We follow several parcels of plasma that are magnetically connected, with footpoint motion included. The first parcel (a) of plasma is emitted at time $t_{a0} = -\delta t/2$ from the faster wind source region with azimuthal angle $\phi_0 + \delta\phi/2$ and colatitude $\theta_0 - \delta\theta/2$. The second parcel (b) of plasma is emitted at time $t_{b0} = \delta t/2$ from the slower source region with azimuthal angle $\phi_0 - \delta\phi/2$ and colatitude $\theta_0 + \delta\theta/2$. Magnetic connection with footpoint motion requires that $\delta\phi = |\omega_\phi|\delta t$ and $\delta\theta = \omega_\theta \delta t$.

The plasma parcels move out ballistically with the solar wind. Therefore, at time t parcel (a) has coordinates

$$r_a = R_B + (V + \delta V/2)(t + \delta t/2) \tag{A.1}$$
$$\theta_a = \theta_0 - \delta\theta/2 \tag{A.2}$$
$$\phi_a = \phi_0 + \delta\phi/2 - \Omega_\odot(t + \delta t/2), \tag{A.3}$$

and parcel (b) has coordinates

$$r_b = R_B + (V - \delta V/2)(t - \delta t/2) \tag{A.4}$$
$$\theta_b = \theta_0 + \delta\theta/2 \tag{A.5}$$
$$\phi_b = \phi_0 - \delta\phi/2 - \Omega_\odot(t - \delta t/2). \tag{A.6}$$

The displacement between parcels (a) and (b) is:

$$\Delta r = r_a - r_b = V\delta t\left(1 + \frac{\delta V}{\delta t}\frac{(r - R_B)}{V^2}\right) \tag{A.7}$$
$$\Delta\theta = \theta_a - \theta_b = -\delta t\omega_\theta \tag{A.8}$$
$$\Delta\phi = \phi_a - \phi_b = -\delta t(\Omega_\odot - |\delta\omega_\phi|). \tag{A.9}$$

We solve for the change in wind speed δV as the footpoint undergoes displacement $\delta\phi$ and $\delta\theta$,

$$\delta V = \left(\frac{\delta V_\phi}{\delta\phi}\right)\delta\phi + \left(\frac{\delta V_\theta}{\delta\theta}\right)\delta\theta$$
$$= \left(\frac{\delta V_\phi}{\delta\phi}\right)|\omega_\phi|\delta t + \left|\frac{\delta V_\theta}{\delta\theta}\right|\omega_\theta\delta t. \tag{A.10}$$

In Eq. (A.10), the terms δV_ϕ and δV_θ refer to the small changes in solar wind speed in the azimuthal and colatitude directions, respectively. By construction both of the directional contributions to δV speed changes are positive since we find the difference between parcel (a) released at time $-\delta t/2$ on a faster stream and parcel (b) released at time $\delta t/2$ on a slower stream. However, δV_θ is a negative quantity, which requires that its contribution to the net speed change is the absolute value of the speed change in the colatitude direction. As a result, we can express the rate of speed change in a more general manner,

$$\frac{\delta V}{\delta t} = -\left(\frac{\delta V_\phi}{\delta\phi}\right)\omega_\phi + \frac{\delta V_\theta}{\delta\theta}\omega_\theta \tag{A.11}$$
$$= -R_B\boldsymbol{\omega}_B \cdot \nabla V|_{r=R_B}, \tag{A.12}$$

where

$$\boldsymbol{\omega}_B = \omega_\theta\hat{e}_\theta + \sin\theta\omega_\phi\hat{e}_\phi. \tag{A.13}$$

We note that the R_B enters the equation but cancels when multiplied by the gradient operator. Further, the quantity $R_B\boldsymbol{\omega}_B$ represents the transverse velocity associated with footpoint motion at the boundary radius R_B. Since the magnetic field must be parallel to the displacement vector, we can solve for the direction of the magnetic field:

$$\boldsymbol{B} = A(\boldsymbol{r})\left\{\left(1 - R_B\boldsymbol{\omega}_B \cdot \nabla V|_{r=R_B}\frac{(r - R_B)}{V^2}\right)\hat{e}_r - \frac{\boldsymbol{\omega}_B r}{V} - \frac{\Omega_\odot r\sin\theta}{V}\hat{e}_\phi\right\}. \tag{A.14}$$

We take the interface between fast and slow wind to be tilted by angle Ψ with respect to the azimuthal direction. On the inner boundary surface, at radius R_B, the unit vector along the stream interface is defined

$$\hat{e}_I = \sin\Psi\hat{e}_\theta + \cos\Psi\hat{e}_\phi. \tag{A.15}$$

On the inner boundary the unit vector normal to the stream interface is defined,

$$\hat{e}_\perp|_{r=R_B} \approx -\cos\Psi\hat{e}_\theta + \sin\Psi\hat{e}_\phi. \tag{A.16}$$

Therefore the footpoint rotation rate normal to the stream interface is

$$\omega_\perp = -\omega_\theta\cos\Psi + \omega_\phi\sin\theta\sin\Psi. \tag{A.17}$$

The footpoint rotation rate times the velocity gradient is

$$R_B\boldsymbol{\omega}_B \cdot \nabla V|_{r=R_B} = \omega_\theta\frac{\partial V}{\partial\theta} + \omega_\phi\frac{\partial V}{\partial\phi} \tag{A.18}$$
$$= R_B\omega_\perp\frac{\partial V}{\partial s_\perp}, \tag{A.19}$$

where the velocity gradient normal to the interface is

$$R_B\frac{\partial V}{\partial s_\perp} = \left(\omega_\theta\frac{\partial V}{\partial\theta} + \omega_\phi\frac{\partial V}{\partial\phi}\right)(-\omega_\theta\cos\Psi + \omega_\phi\sin\theta\sin\Psi)^{-1}. \tag{A.20}$$

In the application to the rarefaction region considered here ω_ϕ is a negative quantity since longitudinal footpoint motion opposes solar rotation, and ω_θ is positive. This implies that $\omega_\perp < 0$,

$$\omega_\perp = -(\omega_\theta\cos\Psi + |\omega_\phi|\sin\theta\sin\Psi). \tag{A.21}$$

The velocity gradient in colatitude is a negative quantity, $\partial V/\partial\theta < 0$, and the velocity gradient in azimuthal is a positive

quantity, $\partial V/\partial\phi > 0$. Therefore, the velocity gradient normal to the interface is a positive quantity,

$$R_{\rm B}\frac{\partial V}{\partial s_\perp} = \left(\omega_\theta\left|\frac{\partial V}{\partial\theta}\right| + |\omega_\phi|\frac{\partial V}{\partial\phi}\right)(\omega_\theta\cos\Psi + |\omega_\phi|\sin\theta\sin\Psi)^{-1}. \tag{A.22}$$

Given these properties of the velocity and footpoint rotation rates, we express the magnetic field in the rarefaction region as follows

$$\boldsymbol{B} = A(\boldsymbol{r})\left\{\left(1 + R_{\rm B}|\omega_\perp|\left.\frac{\partial V}{\partial s_\perp}\right|_{r=R_{\rm B}}\frac{(r-R_{\rm B})}{V^2}\right)\hat{e}_r - \frac{\omega_{\rm B} r}{V} - \frac{\Omega_\odot r\sin\theta}{V}\hat{e}_\phi\right\}. \tag{A.23}$$

We solve for the magnitude A of the magnetic field in the same manner as detailed by Schwadron (2002) by requiring conservation of magnetic flux across the interface between fast wind and the rarefaction region. The unit vector along a fast wind streamline is

$$\hat{e}_{\rm s} = \left(\hat{e}_r - \hat{e}_\phi\Omega_\odot r\sin\theta/V\right)\left(1 + (\Omega_\odot r\sin\theta/V)^2\right)^{-1/2}. \tag{A.24}$$

The unit vector perpendicular to the stream interface $\hat{e}_I$ and perpendicular to the streamline is

$$\hat{e}_\perp(r) = \left(\Omega_\odot r\sin\theta\sin\Psi\hat{e}_r - V\cos\Psi\hat{e}_\theta + V\sin\Psi\hat{e}_\phi\right) \times\left(\Omega_\odot^2 r^2\sin^2\theta\sin^2\Psi + V^2\right)^{-1/2}. \tag{A.25}$$

The magnetic field on the side of the interface with fast solar wind follows a pattern close to the Parker spiral but modified to account for footpoint motion:

$$\boldsymbol{B}_{\rm f} = B_{\rm fB}\left(\frac{R_{\rm B}}{r}\right)^2\left(\hat{e}_{\rm r} - \frac{\omega_{\rm B} r}{V} - \frac{\Omega_\odot r\sin\theta}{V}\hat{e}_\phi\right), \tag{A.26}$$

where $B_{\rm fB}$ is the magnetic field strength on the inner boundary surface. The magnetic field on the rarefaction side of the interface is consistent with Eq. (A.26):

$$\boldsymbol{B}_{\rm a} = A(\boldsymbol{r})\left\{\left(1 + R_{\rm B}|\omega_\perp|\left.\frac{\partial V}{\partial s_\perp}\right|_{r=R_{\rm B}}\frac{(r-R_{\rm B})}{V^2}\right)\hat{e}_{\rm r} - \frac{\omega_{\rm B} r}{V} - \frac{\Omega_\odot r\sin\theta}{V}\hat{e}_\phi\right\}. \tag{A.27}$$

We require conservation of magnetic flux across the interface: $\boldsymbol{B}_{\rm f}\cdot\hat{e}_\perp = \boldsymbol{B}_{\rm a}\cdot\hat{e}_\perp$. Therefore,

$$A(r) = B_{\rm fB}\left(\frac{R_{\rm B}}{r}\right)^2\left(1 + R_{\rm B}\left.\frac{\partial V}{\partial s_\perp}\right|_{r=R_{\rm B}}\frac{(r-R_{\rm B})}{V^2}\Omega_\odot\sin\theta\sin\Psi\right)^{-1}. \tag{A.28}$$

In the treatment of footpoint motion used in this paper, we use the following parameters (adapted from Schwadron 2002):

$$\omega_\theta = 0.1\Omega_\odot$$
$$\omega_\phi = 0.17\Omega_\odot. \tag{A.29}$$

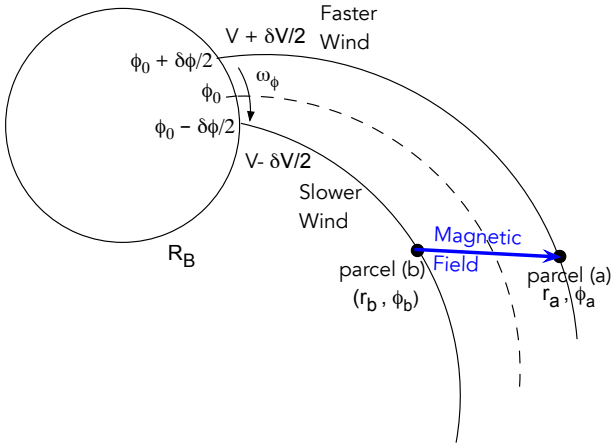

Fig. A.1. Differential motion creates the sub-Parker spiral. Black-curves show the streamlines associated with parcel (a) and parcel (b) in the corotating reference frame. Footpoint motion provides a magnetic connection between parcel (a) and (b), which implies that the magnetic field is directed along the displacement between these plasma parcels.

We introduce the term α to quantify the radial speed gradient within the rarefaction region,

$$\alpha = R_{\rm B}|\omega_\perp|\left.\frac{\partial V}{\partial s_\perp}\right|_{r=R_{\rm B}}. \tag{A.30}$$

Note that α represents an effective acceleration and has units of speed over time (or km s^{-2}). At the position of PSP, the stream interface rotates past the spacecraft at an angular rate of $\Omega_\odot$. Given an observed reduction in solar wind speed of 55 km s^{-1} in 6 days (after the passage of the stream interface), we find a value of $\alpha = 1.8\times10^{-5}$ km s^{-2}.

Appendix B: Distance to the SIR compression or shock

In this appendix, we consider a spacecraft located at a specified set of heliographic coordinates $(r_{\rm o}, \theta_{\rm o}, \phi_{\rm o})$ and derive expressions for the coordinates $(r_{\rm s}, \theta_{\rm s}, \phi_{\rm s})$ where the solar wind magnetic field connects the observer to the SIR compression or shock. We begin by considering these expressions for a standard Parker spiral. The SIR is created by the interaction of a slower and faster streams, with speeds $V_{\rm l}$ and $V_{\rm h}$, respectively. In the corotating coordinate system, the faster stream has the following pathline solution:

$$r(\phi) = r_{\rm o} - \frac{(\phi-\phi_{\rm o})V_{\rm o}}{\Omega_\odot} \tag{B.1}$$
$$\theta = \theta_{\rm o}, \tag{B.2}$$

where $V_{\rm o}$ is the speed at the observer's position. We take the compression or shock to move out with intermediate speed $V_{\rm m} = (V_{\rm l} + V_{\rm h})/2$ and the associated pathline is given by:

$$r_{\rm m}(\phi) = r_{\rm o} - \frac{(\phi-\phi_{\rm m})V_{\rm m}}{\Omega_\odot} \tag{B.3}$$
$$\theta = \theta_{\rm o}. \tag{B.4}$$

where we use $\phi_{\rm m}$ to represent the azimuthal angle of the initial stream interface. The intersection of these pathlines occurs at radius:

$$r_{\rm sh} = r_{\rm o} + \frac{(\phi_{\rm m}-\phi_{\rm o})}{\Omega_\odot}\frac{V_{\rm m}V_{\rm o}}{V_{\rm o}-V_{\rm m}}. \tag{B.5}$$

In the more general case of the sub-Parker spiral in the rarefaction region, the pathline is solved for using the following differential form:

$$\frac{\mathrm{d}r}{\mathrm{d}s} = \frac{A}{B}\left(1 + R_\mathrm{B}|\omega_\perp|\left.\frac{\partial V}{\partial s_\perp}\right|_{r=R_\mathrm{B}}\frac{(r-R_\mathrm{B})}{V^2}\right) \tag{B.6}$$

$$\frac{\mathrm{d}\theta}{\mathrm{d}s} = -\frac{A}{B}\frac{\omega_\theta}{V} \tag{B.7}$$

$$\frac{\mathrm{d}\phi}{\mathrm{d}s} = -\frac{A}{B}\frac{\Omega_\odot - |\omega_\phi|}{V}. \tag{B.8}$$

To solve the parametric pathline equations explicitly, we express the differential distance along the field-line as, $\mathrm{d}s = (VB/A)\mathrm{d}\tau$. The pathline now takes the form

$$\frac{\mathrm{d}r}{\mathrm{d}\tau} = V + \alpha(r - R_\mathrm{B})/V \tag{B.9}$$

$$\frac{\mathrm{d}\theta}{\mathrm{d}\tau} = -\omega_\theta \tag{B.10}$$

$$\frac{\mathrm{d}\phi}{\mathrm{d}\tau} = -(\Omega_\odot - |\omega_\phi|). \tag{B.11}$$

The quantity $\mathrm{d}\tau$ represents an infinitesimal displacement in time along a fieldline history. The equation for r is solved by introducing the displacement with respect to the inner boundary, $R = r - R_\mathrm{B}$, and expressing (B.9) as follows,

$$\exp\left(\int_0^\tau \frac{\alpha}{V}\mathrm{d}\tau'\right)\frac{\mathrm{d}}{\mathrm{d}\tau}\left[\exp\left(-\int_0^\tau \frac{\alpha}{V}\mathrm{d}\tau'\right)R\right] = V. \tag{B.12}$$

The solution is

$$R(\tau) = R_\mathrm{o}\exp\left(\int_0^\tau \frac{\alpha}{V}\mathrm{d}\tau'\right) + \int_0^\tau V\exp\left(\int_{\tau'}^\tau \frac{\alpha}{V}\mathrm{d}\tau''\right)\mathrm{d}\tau'. \tag{B.13}$$

where $R_\mathrm{o} = r_\mathrm{o} - R_\mathrm{B}$. We take α = constant.

The footpoints of the fieldline on the corotating inner boundary have coordinates

$$\theta_\mathrm{B}(\tau) = \theta_\mathrm{Bo} - \omega_\theta\tau \tag{B.14}$$

$$\phi_\mathrm{B}(\tau) = \phi_\mathrm{Bo} - \omega_\phi\tau \tag{B.15}$$

$$= \phi_\mathrm{Bo} + |\omega_\phi|\tau, \tag{B.16}$$

where $(\theta_\mathrm{Bo}, \phi_\mathrm{Bo})$ are the coordinates of the footpoint on the inner boundary associated with fieldline tied to the observer. The velocity along the fieldline history is

$$\begin{aligned} V(\tau) &= V(R_\mathrm{B}, \theta_\mathrm{Bo} - \omega_\theta\tau, \phi_\mathrm{Bo} - \omega_\phi\tau) \\ &\approx V_\mathrm{o} - \tau R_\mathrm{B}\boldsymbol{\omega}_\mathrm{Bo}\cdot\nabla V|_{r=R_\mathrm{B}} \\ &\approx V_\mathrm{o} + \tau\alpha, \end{aligned} \tag{B.17}$$

where $V_\mathrm{o} = V(R_\mathrm{B}, \theta_\mathrm{Bo}, \phi_\mathrm{Bo})$ is the solar wind velocity at the observer location. Therefore, from Eq. (A.10)

$$V(\tau) = V_\mathrm{o} + \alpha\tau. \tag{B.18}$$

With this explicit form of the velocity, the integrals in Eq. (B.13) are directly solved, resulting in the following expression for the fieldline's radial location $R(\tau)$:

$$R(\tau) = R_\mathrm{o}\left(1 + \frac{\alpha\tau}{V_\mathrm{o}}\right) + (V_\mathrm{o} + \alpha\tau)\tau. \tag{B.19}$$

We now solve for the point of intersection of the stream interface with the fieldline in the rarefaction region by equating the azimuthal angle of the stream interface, ϕ_I, with the azimuthal angle along the magnetic field line:

$$\begin{aligned} \phi_\mathrm{I} &= \phi_\mathrm{m} - \frac{\Omega_\odot(R - R_\mathrm{o})(\tau_\mathrm{s})}{V_\mathrm{m}} \\ \phi(\tau_\mathrm{i}) &= \phi_\mathrm{o} - (\Omega_\odot - |\omega_\phi|)\tau_\mathrm{s}, \end{aligned} \tag{B.20}$$

where ϕ_m is the azimuthal location of the stream interface at $R = R_\mathrm{o}$ and $\tau = \tau_\mathrm{s}$ is the traceback time at the intersection point. We then use Eq. (B.19) to convert Eq. (B.20) into a quadratic equation for τ:

$$a\tau_\mathrm{s}^2 + b\tau_\mathrm{s} - \Delta\phi = 0, \tag{B.21}$$

where $\Delta\phi = \phi_\mathrm{m} - \phi_\mathrm{o}$, $a = \Omega_\odot\alpha/V_\mathrm{m}$, and $b = -(\Omega_\odot - |\omega_\phi|) + (R_\mathrm{o}\alpha/V_\mathrm{o} + V_\mathrm{o})\Omega_\odot/V_\mathrm{m}$. In the limit that $\alpha = 0$, Eq. (B.21) yields the solution $\tau_\mathrm{s} = \Delta\phi/[\Omega_\odot(V_\mathrm{o}/V_\mathrm{m} - 1) + |\omega_\phi|]$. This particular solution yields an intersection at r_s given by Eq. (B.5) in the limit of small $|\omega_\phi|$. In the more general case that $\alpha > 0$, we find that

$$\tau_\mathrm{s} = \frac{-b + \sqrt{b^2 + 4a\Delta\phi}}{2a}. \tag{B.22}$$

Given the solutions derived for the radial location of the connection to the compression or shock, we calculate the corresponding distance along the fieldline. In the case of the Parker field structure, the fieldline distance is calculated using

$$\frac{\mathrm{d}s}{\mathrm{d}r} = \frac{B}{B_\mathrm{r}} = \sqrt{1 + r^2\left(\frac{\Omega_\odot\sin\theta}{V}\right)^2}. \tag{B.23}$$

The integral form of Eq. (B.23) is as follows,

$$\Delta s = \frac{V}{\Omega_\odot\sin\theta}\int_{x_\mathrm{o}}^{x_\mathrm{s}}\sqrt{1 + x^2}\mathrm{d}x \tag{B.24}$$

$$= \frac{V}{\Omega_\odot\sin\theta}\left[\frac{x_\mathrm{s}\sqrt{1+x_\mathrm{s}^2}}{2} - \frac{x_\mathrm{o}\sqrt{1+x_\mathrm{o}^2}}{2} + \frac{1}{2}\ln\left(\frac{x_\mathrm{s} + \sqrt{1+x_\mathrm{s}^2}}{x_\mathrm{o} + \sqrt{1+x_\mathrm{o}^2}}\right)\right], \tag{B.25}$$

where $x_\mathrm{o} = r_\mathrm{o}\Omega_\odot\sin\theta/V$ and $x_\mathrm{s} = r_\mathrm{s}\omega_\odot\sin\theta/V$. In the case of the magnetic field that includes footpoint motion, the differential equation along the magnetic field line is solved for using the quantity $\mathrm{d}s/\mathrm{d}\tau$:

$$\frac{\mathrm{d}s}{\mathrm{d}\tau} = \sqrt{\left(\frac{\mathrm{d}r}{\mathrm{d}\tau}\right)^2 + r^2\left(\frac{\mathrm{d}\theta}{\mathrm{d}\tau}\right)^2 + r^2\sin^2\theta\left(\frac{\mathrm{d}\phi}{\mathrm{d}\tau}\right)^2} \tag{B.26}$$

$$= \sqrt{(V + \alpha R/V)^2 + r^2\omega_\theta^2 + r^2\sin^2\theta\left(\Omega_\odot - |\omega_\phi|\right)^2}, \tag{B.27}$$

where $r(\tau) = R(\tau) + R_\mathrm{B}$, and $V(\tau)$ and $R(\tau)$ are specified by Eqs. (B.18) and (B.19). The resulting relation for the distance along the fieldline is,

$$\Delta s = \int_0^{\tau_\mathrm{s}}\mathrm{d}\tau\left[(V + \alpha R/V)^2 + r^2\omega_\theta^2 + r^2\sin^2\theta\left(\Omega_\odot - |\omega_\phi|\right)^2\right]^{1/2}. \tag{B.28}$$

A special case to consider is where $\alpha = 0$ and the previous expression for the Δs can be made explicit:

$$\Delta s = \frac{V}{|\omega|}\left[\frac{x'_s\sqrt{1+(x'_s)^2}}{2} - \frac{x'_o\sqrt{1+(x'_o)^2}}{2} + \frac{1}{2}\ln\left(\frac{x'_s+\sqrt{1+(x'_s)^2}}{x'_o+\sqrt{1+(x'_o)^2}}\right)\right], \tag{B.29}$$

where $x'_o = r_o|\omega|/V$, $x'_s = r_s|\omega|/V$ and

$$|\omega| = \sqrt{\omega_\theta^2 + \sin^2\theta(\Omega_\odot - |\omega_\phi|)^2}. \tag{B.30}$$

In the case of the magnetic field that includes footpoint motion, the differential equation along the magnetic field line is solved

Appendix C: Injection energy into diffusive shock acceleration

The injection energy is determined by the angle between the magnetic field and the shock normal. The shock normal is solved using Eq. (B.5) for the shock radius. This yields a shock or compression normal given by

$$\hat{e}_{sn} = \frac{(r\sin\theta/L_s)\hat{e}_r + \hat{e}_\phi}{\sqrt{(r\sin\theta/L_s)^2+1}}, \tag{C.1}$$

where

$$L_s = \frac{V_h}{\Omega_\odot}\frac{V_h+V_l}{V_h-V_l}. \tag{C.2}$$

With $V_l = 320$ km s^{-1} and $V_h = 530$ km s^{-1}, we find that $L_s = 5.1$ au. The unit vector along the magnetic field in the fast solar wind upstream of the shock or compression is

$$\hat{e}_B = \left\{\left(1+\alpha\frac{(r-R_B)}{V^2}\right)\hat{e}_r - \frac{\omega_\theta r}{V}\hat{e}_\theta - \frac{(\Omega_\odot+\omega_\phi)r\sin\theta}{V}\hat{e}_\phi\right\} \times\left\{\left(1+\alpha\frac{(r-R_B)}{V^2}\right)^2 + \left(\frac{\omega_\theta r}{V}\right)^2 + \left(\frac{(\Omega_\odot+\omega_\phi)r\sin\theta}{V}\right)^2\right\}^{-1/2}. \tag{C.3}$$

The unit vector along the magnetic field for a Parker spiral is given by,

$$\hat{e}_B = \left\{\hat{e}_r - \frac{\Omega_\odot r\sin\theta}{V}\hat{e}_\phi\right\}\left\{1+\left(\frac{\Omega_\odot r\sin\theta}{V}\right)^2\right\}^{-1/2}. \tag{C.4}$$

The injection speed v_{inj} (and associated injection energy) is found from the condition that the energetic particle anisotropy is sufficiently small (Giacalone 2001):

$$v_{inj} = u_1\left[1+\frac{(\kappa_A/\kappa_\parallel)^2\sin^2\theta_1 + (1-\kappa_\perp/\kappa_\parallel)^2\sin^2\theta_1\cos^2\theta_1}{\left((\kappa_\perp/\kappa_\parallel)\sin^2\theta_1+\cos^2\theta_1\right)^2}\right]^{1/2}, \tag{C.5}$$

where $\kappa_A = vr_g/3$, r_g is the gyroradius, u_1 is the upstream solar wind speed, and θ_1 is the upstream angle between the magnetic field and the shock normal. In the limit that $\kappa_A \to 0$ and $\kappa_\perp/\kappa_\parallel \to 0$, the injection speed becomes, $v_{inj} = u_1/\cos\theta_1$, which is the speed of shock (or compression) along a magnetic flux tube. Only ions with a speed larger than injection speed can move upstream relative to the shock or compression and thereby gain energy through multiple crossings of the speed gradient in the bulk plasma. Therefore, the injection speed acts as a gate for ions to begin the diffusive acceleration process.

Appendix D: Rates associated with acceleration and cooling of SIR suprathermal populations

Observations have shown that there is a common form of the particle energy distribution within SIRs, as detailed in the introduction. This form of the distribution may be the result of the superposition of distribution functions from distributed sources (Schwadron et al. 2010), or from specific acceleration mechanisms. Given the form of the energy distribution (1), and the relatively low injection energy (<1 keV, Fig. 3, panel 4), it is expected that particle acceleration at energies near the injection energy increases the magnitude of the distribution function with distance. In the corotating reference frame, the steady-state evolution of the isotropic part of the distribution function $\tilde{f}_s$ at speeds v with associated speed $v > u$ but near injection is approximated (Fisk 1976; Schwadron et al. 1996):

$$\boldsymbol{u}\cdot\nabla\tilde{f}_s - \frac{1}{3}\nabla\cdot\boldsymbol{u}\,p\frac{\partial\tilde{f}_s}{\partial p} - \frac{1}{p^2}\frac{\partial}{\partial p}\left(p^2 D_{pp}\frac{\partial\tilde{f}_s}{\partial p}\right) = 0, \tag{D.1}$$

where $\boldsymbol{u}$ is the bulk-flow velocity in the corotating reference frame, p is the particle momentum, and D_{pp} is the diffusion term in momentum space, which takes into account wave-particle interactions resulting in effects such as transit-time damping (Fisk 1976; Schwadron et al. 1996). Note that this form of the Parker transport equation neglects diffusion due to the low mobility of ions for ion speeds that slightly exceed the bulk wind speed (e.g., $1 < v/u \leq 5$ in the plasma frame, where u is the radial solar wind speed). We take the distribution function within the SIR near the injection energy to depend on particle speed and radial distance, $\tilde{f}_s(r, v)$, with the functional form for the speed detailed in the introduction (see Eq. (1)). The speeds indicated here are below the exponential roll-over. Therefore,

$$\tilde{f}_s \approx F_s(r)v^{\gamma_s}. \tag{D.2}$$

Substitution of Eq. (D.2) into the transport Eq. (D.1) and averaging over the SIR longitude at a given radius yields

$$u\frac{\partial F_s}{\partial r} - \dot{a}_s F_s = 0, \tag{D.3}$$

where the rate associated with acceleration is defined

$$\dot{a}_s = \gamma_s\langle\nabla\cdot\boldsymbol{u}\rangle_s/3 + \gamma_s^2\frac{D_{pp}}{p^2} + \gamma_s\frac{1}{p^2}\frac{\partial}{\partial p}\left(pD_{pp}\right). \tag{D.4}$$

The averaging within the SIR is indicated by $\langle\ldots\rangle_s$. The solution to Eq. (D.3) yields the following approximation

$$F_s \propto \exp\left(\frac{\dot{a}_s r}{u}\right). \tag{D.5}$$

The net cooling rate is scaled in terms of the solar wind expansion. We use an expansion factor g such that

$$\nabla\cdot\boldsymbol{u} = gu/r. \tag{D.6}$$

For example, with a radial expansion, $g = 2$. The transport equation in this case is

$$\boldsymbol{u} \cdot \nabla \tilde{f}_\mathrm{s} - \frac{g}{3}\frac{u}{r} p \frac{\partial \tilde{f}_\mathrm{s}}{\partial p} = 0. \tag{D.7}$$

The resulting equation for the radial dependence of the distribution is

$$u\frac{\partial F_\mathrm{s}}{\partial r} - \frac{g\gamma_\mathrm{s}}{3}\frac{u}{r}F_\mathrm{s} = 0, \tag{D.8}$$

which has the solution,

$$F_\mathrm{s} \propto r^{g\gamma_\mathrm{s}/3}. \tag{D.9}$$

We use the results in Eqs. (D.5) and (D.9) to solve for the distribution function f_s in SIRs throughout the inner heliosphere:

$$f_\mathrm{s} = F_\mathrm{s}(r)(v/u_\mathrm{s})^{\gamma_\mathrm{s}} \exp[-(v-u_\mathrm{s})/v_\mathrm{s}], \tag{D.10}$$

where u is the intermediate solar wind speed in the SIR

$$\begin{aligned} F_\mathrm{s}(r) &= F_\mathrm{peak} \exp[(r - r_\mathrm{peak})\dot{a}_\mathrm{s}/u_\mathrm{s}] \ \text{ for } \ r \le r_\mathrm{peak} \\ &= F_\mathrm{peak}(r/r_\mathrm{peak})^{g\gamma_\mathrm{s}/3} \ \text{ for } \ r > r_\mathrm{peak}. \end{aligned} \tag{D.11}$$

The radial location r_peak of the peak distribution function associated with the radial distance where the forward or reverse shock moves through the extent of either slower wind in front of the SIR or the faster wind behind the SIR. The peak in the distribution function, F_peak, is related to the injection of pickup ions at $r = r_\mathrm{peak}$ (Schwadron et al. 1996):

$$F_\mathrm{peak} = \frac{3n_\mathrm{H}\beta_1}{8\pi u_\mathrm{s}^4}\left(\frac{r_1^2}{r_\mathrm{peak}}\right)\epsilon, \tag{D.12}$$

where ϵ is a peak injection efficiency, $r_1 = 1$ AU, β_1 is the ionization rate referenced to 1 AU, and the neutral interstellar H density is

$$n_\mathrm{H} \approx n_\mathrm{H0} \exp(-\lambda_\mathrm{H}/r_\mathrm{peak}). \tag{D.13}$$

Here, the hydrogen density in the outer heliosphere is $n_\mathrm{H0} = 0.1$ cm^{-3}, we take $\lambda_\mathrm{H} = 4$ AU and $\beta_1 = 6 \times 10^{-7}$ s^{-1}. Note that the term ϵ scales the height of the suprathermal tail relative to the injected pickup ion population. In principle the peak injection efficiency ϵ should be close to 1.

Appendix E: Particle transport through the rarefaction region

The Parker transport equation is written as follows,

$$\frac{\partial f}{\partial t} + \boldsymbol{u} \cdot \nabla f - \nabla \cdot (\bar{\bar{\kappa}} \cdot \nabla f) - \frac{1}{3}\nabla \cdot \boldsymbol{u} p \frac{\partial f}{\partial p} = Q. \tag{E.1}$$

We transform the transport equation into the corotating frame where the bulk flow velocity in this frame is $\boldsymbol{u}' = \boldsymbol{u} + \boldsymbol{r}' \times \boldsymbol{\Omega}_\odot$:

$$\frac{\partial f}{\partial t} + \boldsymbol{u}' \cdot \nabla' f - \nabla' \cdot (\bar{\bar{\kappa}} \cdot \nabla' f) - \frac{1}{3}\nabla' \cdot \boldsymbol{u}' p \frac{\partial f}{\partial p} = Q. \tag{E.2}$$

We invoke steady state in the corotating reference frame, and take the solar wind to be radial in the inertial frame, $\boldsymbol{u} = u\hat{e}_r$. Accordingly, in the corotating reference frame, the solar wind velocity is $\boldsymbol{u}' = u\hat{e}_r - \Omega_\odot r \sin\theta \hat{e}_\phi$ and the transport equation in this system is

$$\boldsymbol{u}' \cdot \nabla' f - \nabla' \cdot (\bar{\bar{\kappa}} \cdot \nabla' f) - \frac{2u}{3r} p \frac{\partial f}{\partial p} = Q. \tag{E.3}$$

We consider diffusive propagation along a fieldline with distance s, and take a fixed power-law in momentum-space, $f \propto p^{-\alpha}$:

$$u_\mathrm{s}\frac{\partial f}{\partial s} - B\frac{\partial}{\partial s}\left(\frac{\kappa_\parallel}{B}\frac{\partial f}{\partial s}\right) - \frac{\partial}{\partial s_\perp}\left(\kappa_\perp \frac{\partial f}{\partial s}\right) + \frac{2u\alpha}{3r} p f = 0, \tag{E.4}$$

where $u_\mathrm{s} = \boldsymbol{u}' \cdot \hat{e}_\mathrm{B}$. Here $s_\perp$ refers to distance along a curve perpendicular to the magnetic field.

We solve the problem numerically by setting up a grid of field lines out to the SIR. Each node location along the grid is specified as a function of radial distance and azimuthal angle. The diffusion equation is solved using second-order differencing across the field-line, and a spectral solution (equivalent to a Fourier transform solution) along the magnetic field. The power-law in momentum space varies across the grid in response to modulation by the solar wind.